Highly efficient binary copper–iron catalyst for photoelectrochemical carbon dioxide reduction toward methane

Baowen Zhou[a,b,1], Pengfei Ou[c,1], Nick Pant[a], Shaobo Cheng[d], Srinivas Vanka[a,b], Sheng Chu[b], Roksana Tonny Rashid[b], Gianluigi Botton[d], Jun Song[c,2], and Zetian Mi[a,b,2]

[a]Department of Electrical Engineering and Computer Science, University of Michigan, Ann Arbor, MI 48109; [b]Department of Electrical and Computer Engineering, McGill University, Montreal, QC H3A0E9, Canada; [c]Department of Mining and Materials Engineering, McGill University, Montreal, QC H3A0C5, Canada; and [d]Department of Materials Science and Engineering, Canadian Centre for Electron Microscopy, McMaster University, Hamilton, ON L8S4M1, Canada

Edited by Richard Eisenberg, University of Rochester, Rochester, New York, and approved December 6, 2019 (received for review July 6, 2019)

A rational design of an electrocatalyst presents a promising avenue for solar fuels synthesis from carbon dioxide (CO_2) fixation but is extremely challenging. Herein, we use density functional theory calculations to study an inexpensive binary copper–iron catalyst for photoelectrochemical CO_2 reduction toward methane. The calculations of reaction energetics suggest that Cu and Fe in the binary system can work in synergy to significantly deform the linear configuration of CO_2 and reduce the high energy barrier by stabilizing the reaction intermediates, thus spontaneously favoring CO_2 activation and conversion for methane synthesis. Experimentally, the designed CuFe catalyst exhibits a high current density of −38.3 mA·cm^{-2} using industry-ready silicon photoelectrodes with an impressive methane Faradaic efficiency of up to 51%, leading to a distinct turnover frequency of 2,176 h^{-1} under air mass 1.5 global (AM 1.5G) one-sun illumination.

binary copper–iron catalyst | CO_2 reduction | methane | photoelectrocatalysis

The production of clean solar fuels from carbon dioxide (CO_2) and water via photoelectrocatalysis (PEC) provides a promising route for alleviating our society's reliance on fossil fuels and reducing atmospheric carbon emissions (1–4). A rational design of an electrocatalyst is the key for achieving high performance of CO_2 reduction reactions (CO_2RR) (5–7). It is worth noting that, among various products formed from PEC CO_2RR, the most reduced methane is highly energy dense (ΔH_C^o = 891 kJ/mol), and its storage, transportation, and combustion are compatible with the existing industrial infrastructure, thus being an ideal solar fuel (8). However, the production of methane requires complicated 8-electron/proton coupling transfer, which is both kinetically and thermodynamically unfavorable (9–11). The development of an efficient electrocatalyst is thus highly desirable (12).

Over the past few decades, a large number of electrocatalysts, including molecular complexes (13, 14), enzymes (15, 16), metals (17, 18), and transition metal chalcogenides (19, 20), have been developed for CO_2RR. Among these materials, copper (Cu) is well known to be a state-of-the-art electrocatalyst for producing methane from CO_2RR (21–27). To date, however, the use of Cu catalyst for PEC methane synthesis (28, 29) has suffered severely from low current density, inferior Faradaic efficiency, low turnover frequency, and high overpotential. This is because Cu with monofunctional site generally possesses a very weak interaction with CO_2, which is not capable of concurrently activating CO_2 molecules and stabilizing the subsequent reaction intermediates (30–32). Recently, binary catalyst of Cu with secondary metals and their derivatives has emerged as a possible approach to enhance the performance of PEC CO_2RR. For example, Chu et al. (33) demonstrated that oxide-derived Cu–Zn electrocatalyst exhibited a remarkable enhancement on tunable syngas formation with a benchmark turnover number of 1,330 compared to Cu alone. Kong et al. (34) described directed assembly of CuAu nanoparticles on silicon nanowire (NW) photoelectrodes, exhibiting an evidently accelerated CO_2-to-CO conversion with high selectivity of 80% at −0.2 V. Yin et al. (35) developed a Cu–Zn alloy for selectively reducing CO_2 toward HCOOH with a Faradaic efficiency of 79.11% through PEC, which is superior to either Zn or Cu. Nevertheless, these reported binary systems are still not efficient at improving the interaction with CO_2 for methane synthesis from PEC CO_2RR. Therefore, a rational design of a novel binary catalyst of Cu for simultaneous CO_2 activation and stabilization of various intermediates to effectively synthesize methane is of fundamental and practical interest (30, 36), but has remained a grand challenge.

In this work, we present the discovery of a binary CuFe electrocatalyst for the selective reduction of CO_2 to CH_4. Density functional theory (DFT) calculations reveal that Cu and Fe in the binary system work in synergy to induce a significantly distorted O–C–O angle of 126.05° from its original linear configuration at the interface to render a strong interaction with CO_2, and a drastic reduction in the reaction energy barrier, thus greatly facilitating methane synthesis. Experimentally, the CuFe binary electrocatalyst is shown to exhibit high current density of −38.3 mA·cm^{-2} for silicon-based photoelectrodes with high

Significance

The production of solar fuels from CO_2 using sunlight and electricity provides one promising route for reducing atmospheric carbon emissions and storing intermittent solar energy. The rational design of an efficient and inexpensive electrocatalyst is the key. We developed a binary copper–iron catalyst for photoelectrochemical CO_2 reduction toward methane. The theoretical calculations suggest that Cu and Fe in the binary system can work in synergy to spontaneously favor CO_2 activation and conversion for methane synthesis. The earth-abundant CuFe catalyst exhibits a high current density with an impressive methane Faradaic efficiency using industry-ready planar silicon photoelectrodes under one-sun illumination. This work presents a unique, highly efficient, and inexpensive route for solar fuels synthesis.

Author contributions: B.Z. and Z.M. designed research; B.Z., N.P., S. Cheng, S.V., R.T.R., and G.B. performed experiments; B.Z. and S. Chu analyzed experimental data; B.Z., P.O., J.S., and Z.M. wrote the paper; P.O. performed DFT calculation; and P.O. and J.S. analyzed calculation results.

The authors declare no competing interest.

This article is a PNAS Direct Submission.

[1]B.Z. and P.O. contributed equally to this work.

[2]To whom correspondence may be addressed. Email: jun.song2@mcgill.ca or ztmi@umich.edu.

This article contains supporting information online at https://www.pnas.org/lookup/suppl/doi:10.1073/pnas.1911159117/-/DCSupplemental.

First published January 3, 2020.

Faradaic efficiency of up to 51% and high turnover frequency (TOF) of 2,176 h^{-1} for PEC CO_2RR toward CH_4 under simulated solar light (air mass 1.5 global [AM 1.5G], 100 mW·cm^{-2}) at −1.2 V versus reversible hydrogen electrode (RHE), which is superior to that of both Cu and Fe catalyst individually. In addition, the photocathode is made entirely of Earth-abundant materials by industrial semiconductor manufacturing process, presenting one promising route for producing clean fuels in aqueous solution using solar energy.

Results

CO_2 Adsorption/Activation over Cu(111) and Fe_xO_y/Cu(111). Since the initial activation of the inert CO_2 is crucial for the subsequent reactions, CO_2 adsorption characteristics were first investigated using DFT calculations. As iron appears to be in its oxidation state, Fe_xO_y was used in the analysis, and the preferred orientation of Cu surface with the lowest surface energy, that is, Cu(111), was adopted. Therefore, an inverse hydrogenated $Fe_3O_6H_6$/Cu(111) was utilized as a representative model for CuFe electrocatalyst (please see *Computational methods* for more details), by taking the aqueous CO_2RR environment (37) and the preferable H spillover from metal particles to oxide support into consideration (38). Illustrated in Fig. 1*A* and Fig. 1*B* are the optimized structures for CO_2 adsorption on Cu(111) and $Fe_3O_6H_6$/Cu(111), respectively. For the case of CO_2 on Cu(111), we see that CO_2 remains the original linear configuration with the O−C−O angle of 179.67°, and the 2 C−O bond lengths are similar to the CO_2 isolated gas phase (Fig. 1*A* and *SI Appendix*, Fig. S1 and Table S1). On the other hand, it is found that, for the case of CO_2 at the $Fe_3O_6H_6$/Cu(111) interface, the C atom strongly binds to the Cu atom underneath, with a bond length of 1.98 Å, and one O atom attaches to the Fe atom with a shorter bond length of 1.96 Å. This signifies a much stronger bonding, which results in a significant distortion of CO_2 away from its original linear form to a bent form with an O−C−O angle of 126.05° (Fig. 1*B* and *SI Appendix*, Table S1). A bidentate configuration is therefore formed, which facilitates the subsequent reactions (36, 39). In addition, it is observed that the interaction of CO_2 with the $Fe_3O_6H_6$/Cu(111) interface weakens the 2 C−O bonds of CO_2, leading to elongated C−O bonds (1.28 and 1.25 Å) from the original bond length of 1.18 Å in an isolated CO_2. The weakened C−O bonds and the distorted CO_2 configuration together highlight an obvious activation of CO_2 upon chemisorption at the interface, which is in stark contrast to the negligible activation of CO_2 on Cu(111) that is highly beneficial for CO_2RR. The CO_2 activation mechanism at Fe_xO_y/Cu(111) interface reveals a similarity to that of individual metal oxide, for example, TiO_2 (38), with surface oxygen vacancies, in which an undercoordinated Fe atom at the edge of the oxide cluster (i.e., essentially an O vacancy) acts as the active center to bind one of the O atom in CO_2 (40, 41). It is also worth noting that the coexistence of iron oxides and Cu nanoparticles facilitates the formation of the bifunctional Fe_xO_y/Cu(111) interface. On one hand, Fe_xO_y/Cu(111) interface allows multiple adsorption sites and directly participates in stabilizing the key reaction intermediates, such as $*CO_2$, $*C_xH_yO_z$, and $*C_xH_y$. On the other hand, the strong interaction between iron oxides and Cu nanoparticles results in a unique electronic structure that differs from those of isolated components, which is suitable for CO_2 activation and its subsequent transformation (39). These results are consistent with the observation in thermal CO_2 catalysis at metal/oxide interface (42–44), and can be further verified by the CO_2 adsorption capacity measurement (*SI Appendix*, Fig. S2) showing much larger CO_2 adsorption capacity of CuFe@GaN NWs/Si than that of Cu/GaN NWs/Si.

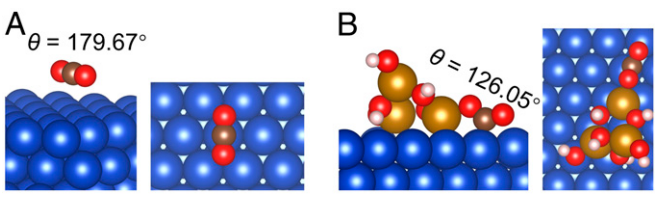

Fig. 1. CO_2 adsorption and activation over Fe_xO_y/Cu(111). Side and top views of optimized configurations of CO_2 activation on Cu(111) (*A*) and $Fe_3O_6H_6$/Cu(111) (*B*). Cu, blue; Fe, orange; O, red; C, brown; and H, white.

Synthesis and Characterization of the Binary CuFe Electrocatalyst. Inspired by the theoretical results above, we developed a binary CuFe catalyst monolithically integrated with GaN NW arrays on planar n^+-p silicon wafer, which was achieved by combing highly controlled molecular beam epitaxy with facile electrodeposition (*SI Appendix*, Fig. S3). As illustrated in Fig. 2*A* and *SI Appendix*, Fig. S4, one-dimensional (1D) GaN NWs are first grown on planar n^+-p silicon junction with a length of ∼300 nm and diameters varying from 30 to 40 nm, using molecular beam epitaxy. Transmission electron microscope (TEM) images show that GaN NWs are nearly defect-free with lattice space of ∼0.26 nm, suggesting the c-axis growth direction (*SI Appendix*, Fig. S5) (33). Using these NWs as support, Cu and Fe were facilely codeposited via electrocatalysis. After the electrodeposition, the morphology of the GaN NW arrays remains largely unchanged (Fig. 2*B*). Scanning TEM high-angle annular dark-field (STEM-HAADF) image and elemental distribution mappings illustrate that both Cu and Fe are clearly dispersed on GaN NW with a unique alloyed geometry (Fig. 2 *C*–*G*). The binary CuFe catalyst loading could be optimized by the 1D GaN NWs. In particular, 1D nanostructure is favorable for exposing cocatalyst with high-density active sites. What is more, the ultrahigh surface-to-volume ratio of 1D nanostructure helps to reduce the loading amount of the catalyst (45). The inductively coupled plasma atomic emission spectrum (ICP-AES) indicates that the content of the binary CuFe catalyst is 0.041 μmol·cm^{-2} with Fe/Cu ratio of 6.3/1. X-ray photoelectron spectroscopy (XPS) measurement was conducted to further analyze the chemical states of Cu and Fe (*SI Appendix*, Fig. S6). It is clearly shown that the characteristic peaks of Cu 2p 3/2 and Cu 2p 1/2 appear at 933.2 and 953.1 eV (Fig. 2*H*), due to metallic copper and/or partially oxidized copper. Meanwhile, the peaks of ∼711 and 725 eV are associated with Fe 2p 3/2 and Fe 2p 1/2, respectively (Fig. 2*I*). As suggested by previous studies, these peaks originate from iron oxides and/or hydroxides (Fe_xO_y/$Fe_x(OH)_y$) (46). X-ray diffraction spectrum measurement in *SI Appendix*, Fig. S7 illustrates that only a featured peak of GaN (002) at ∼34° was observed for both GaN/Si and CuFe@GaN NWs/Si (33). This may originate from both the low content of Cu and Fe and their amorphous phase, which agree well with TEM and ICP-AES characterizations. The amorphous copper−iron catalyst supported on one-dimensional GaN NW arrays could provide sufficient surface defects as well as a large number of low-coordinated atoms of the catalyst, and, consequently, abundant active sites can be produced for CO_2RR (47, 48).

Photoelectrochemical CO_2 Reduction Reaction. The PEC CO_2RR performance of CuFe@GaN NWs/Si as well as other photocathodes was examined in CO_2-saturated 0.5 mol/L $KHCO_3$ aqueous solution. As shown in Fig. 3*A*, it is obvious that, among all 5 of the tested photocathodes, CuFe@GaN NWs/Si exhibits the best current density–voltage (*J*–*V*) curve under standard one-sun illumination. Compared to bare n^+-p silicon junction, GaN NWs/Si shows an evidently improved *J*–*V* curve with an onset potential of −0.33 V (corresponding to a current density of −0.1 mA·cm^{-2}) but still suffers from rapid surface recombination and slow reaction kinetics because of the lack of catalysts. The introduction of catalysts could significantly improve the *J*–*V* behavior. It is noted

CHEMISTRY

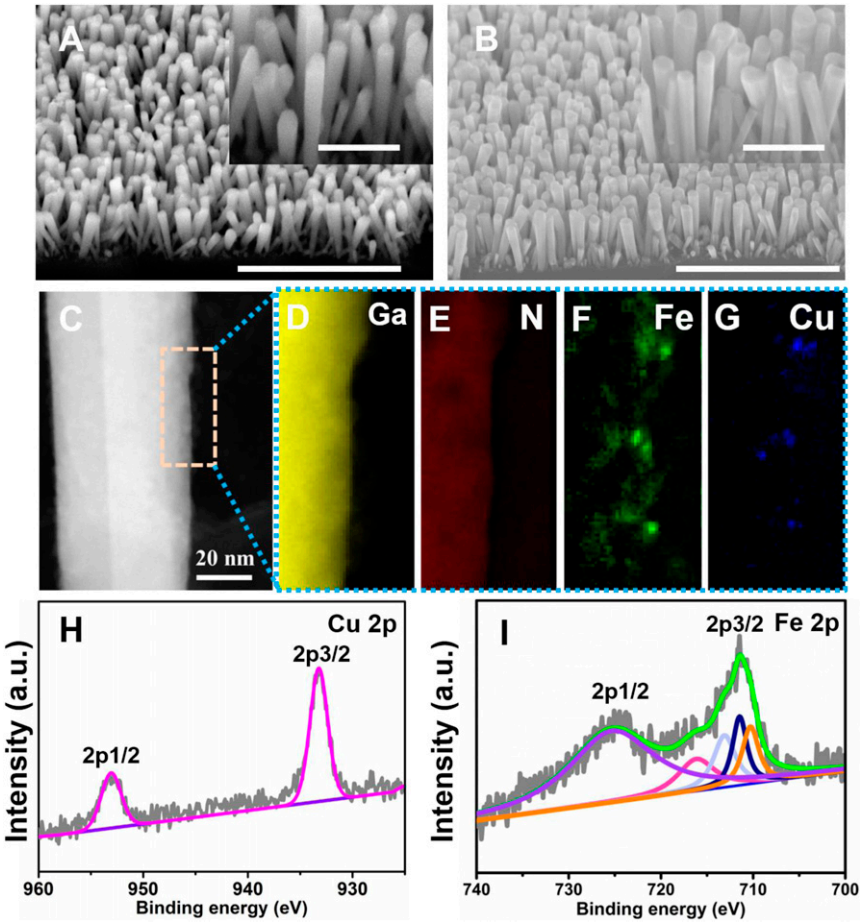

Fig. 2. Structure and chemical characterization. Scanning electron microscopy (SEM) images of bare GaN NWs/Si (*A*) and CuFe@GaN NWs/Si (*B*) with magnified *Insets*. (Scale bars: *A* and *B*, 1 μm; *Insets*, 500 nm.) STEM-HAADF image of GaN nanowire NW modified with binary CuFe catalyst (*C*). The elemental distribution mappings of Ga (*D*), N (*E*), Fe, (*F*) and Cu (*G*) are described as well; the full horizontal width of *D*–*G* is 20 nm. XPS measurement of Cu 2p (*H*) and Fe 2p (*I*) in CuFe@GaN NWs/Si. a.u. denotes arbitrary unit; in *H*, the gray and pink lines represent original and fitting data of Cu 2p, respectively; in *I*, the gray and green lines represent original and fitting data of Fe 2p while orange, deep blue, light blue, pink, and purple lines represent various iron oxides and/or hydroxides.

that the binary CuFe catalyst shows an obvious enhancement compared to both Fe and Cu individually, confirming the synergetic effect of Cu and Fe for the reaction. The superior onset potential of +0.23 V of CuFe@GaN NWs/Si is 200 and 290 mV higher than that of Fe/GaN NWs/Si and Cu/GaN NWs/Si, respectively. Importantly, the current density of CuFe@GaN NWs/Si reaches −38.3 mA·cm^{-2} at −1.2 V, which is close to the light-limited current of the silicon-based photocathode (~−45 mA·cm^{-2}) under one-sun illumination (49). The origin of the improved performance comes primarily from the fact that the CuFe catalyst offers active centers to promote the kinetics (8). Moreover, photoluminescence (PL) spectra in *SI Appendix*, Fig. S8 illustrate that the featured peak intensity decreased in the order of GaN NWs/Si > Cu/GaN NWs/Si > CuFe@GaN NWs/Si. It indicates that a Schottky junction is formed between the loaded cocatalysts and GaN semiconductor, which is capable of greatly promoting the electron−hole separation (50). Furthermore, the dramatic reduction in PL intensity of CuFe@GaN NWs as compared to Cu/GaN NWs suggests that the binary CuFe catalyst is more favorable than Cu catalyst to promote electron−hole separation of GaN NWs. Additionally, it is found that the light intensity affected the *J*–*V* curve significantly (*SI Appendix*, Fig. S9). The current density increased with the increasing intensity because more electron−hole pairs could be formed under illumination with higher intensity. In contrast, there is nearly no current observed in the dark during the entire potential range examined. These results suggest that light-driven generation of electron−hole pairs is a critical step for CO_2RR. Moreover, control experiments confirm that the linear sweep voltammetry (LSV) behavior under CO_2 atmosphere is superior to that under argon atmosphere (*SI Appendix*, Fig. S10), which further suggests the strong adsorption and activation of CO_2 over the binary CuFe catalyst (39). Based on Faradaic efficiency measurements, both GaN NWs/Si and Fe/GaN NWs/Si do not produce any methane (Fig. 3*B*). Hydrogen was the main byproduct, with a trace amount of CO (Faradaic efficiency <1%). Although Cu is catalytically active for methane synthesis, Cu/GaN NWs/Si only shows a low Faradaic efficiency of ~20%, which is consistent with previous work (28). In stark contrast, the binary CuFe catalyst gives rise to more than 2-fold improvement in Faradaic efficiency, to 51% with a high current density of −38.3 mA·cm^{-2}. As a consequence, the partial current density of CuFe@GaN NWs/Si for CH_4 formation is as high as −19.5 mA·cm^{-2} (Fig. 3*C*), which is remarkably higher than the previously reported silicon photocathode for PEC CO_2RR toward CH_4 (28, 29). The optimal productivity of CuFe@GaN NWs/Si for CH_4 approaches 88.8 μmol·h^{-1}·cm^{-2}, which is 3.7 times larger than that of Cu/GaN NWs/Si, while Fe/GaN NWs/Si did not show any productivity under the same experimental conditions (Fig. 3*D*). These results undoubtedly suggest that the binary CuFe catalyst plays a crucial role in promoting methane production. Electronic properties evaluation of Cu using X-ray photoelectron spectrum demonstrates a considerable shift of about +0.3 eV. Cu 2p 3/2 was

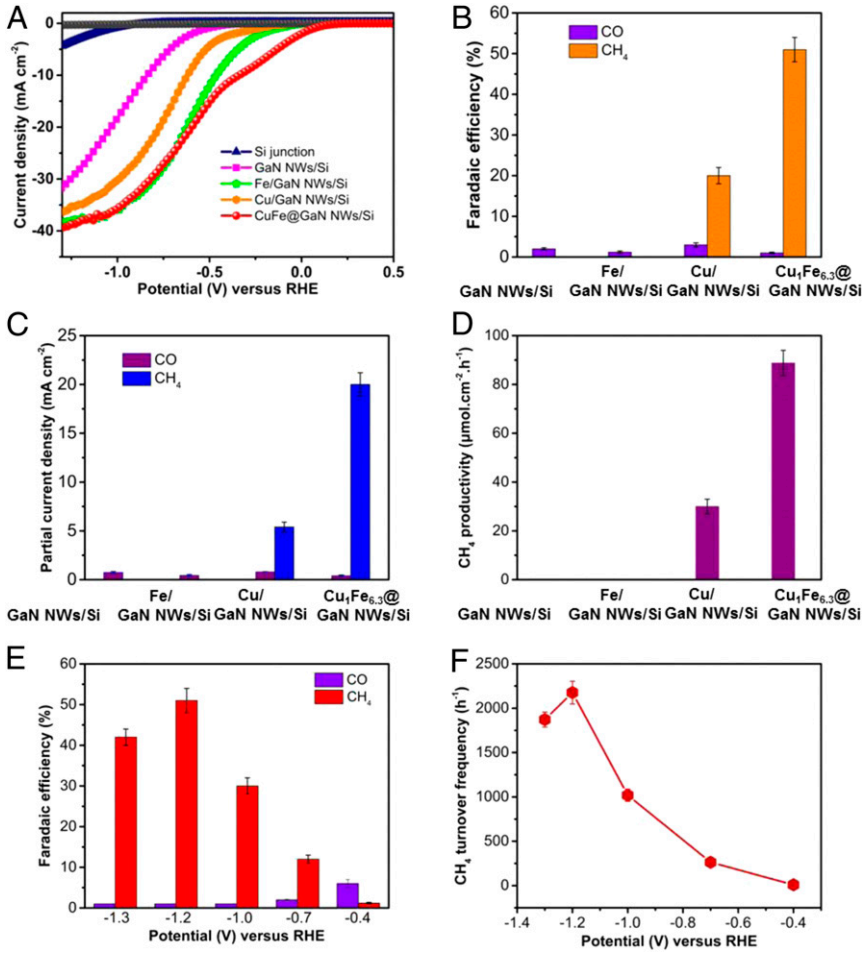

Fig. 3. Photoelectrocatalytic performance measurements. *J*–*V* curves (*A*), Faradaic efficiencies (*B*), partial current density (*C*), and CH_4 productivity (*D*) of GaN NWs/Si, Cu/GaN NWs/Si, Fe/GaN NWs/Si, and CuFe@GaN NWs/Si. The gray curve in *A* corresponds to CuFe@GaN NWs/Si under dark. Variations of Faradaic efficiencies (*E*) and turnover frequency (*F*) for methane synthesis versus applied bias for CuFe@GaN NWs/Si. Experimental conditions: CO_2-purged 0.5 M $KHCO_3$ aqueous solution (pH ≈ 8), one-sun illumination (AM 1.5G, 100 mW·cm^{-2}).

shifted from 932.9 to 933.2 eV by incorporating Fe species, suggesting that Cu in CuFe@GaN NWs/Si is electron-deficient compared to Cu/GaN NWs/Si (*SI Appendix*, Fig. S11) (51). Such a notable change of electronic properties may contribute to tuning the catalytic properties of Cu (52), and thus facilitates the CO_2RR toward methane. It is noted that there is an optimized CuFe catalyst for maximum activity and methane selectivity. At a low loading amount of ∼0.033 μmol·cm^{-2} with Fe/Cu ratio of 4.5/1 (*SI Appendix*, Fig. S12), the active sites of CuFe@GaN NWs/Si are insufficient for suppressing charge carrier surface recombination and improving the kinetics, resulting in limited activity (7). However, at higher Fe/Cu ratio of 12.9/1 with CuFe overloading of 0.075 μmol·cm^{-2} (*SI Appendix*, Fig. S13), the light absorption of the silicon semiconductor would be suppressed (53), and the inherent catalytic activities would be lowered (54) (*SI Appendix*, Figs. S14 and S15). Therefore, there is an appropriate loading amount of 0.041 μmol·cm^{-2} with Fe/Cu ratio of 6.3/1, enabling optimal optical and catalytic activity for highly efficient PEC CO_2RR toward CH_4.

The dependence of Faradaic efficiency on the applied potentials is studied, and the results are illustrated in Fig. 3*E*. It is discovered that the applied potentials play a significant role in the Faradaic efficiency. The onset of CuFe@GaN NWs/Si for methane synthesis is −0.4 V with a methane Faradaic efficiency of 1.2%, which is more positive than that of −0.7 V for Cu alone. It reveals that a significantly lower driving force (by as much as 0.3 V) is required for the binary CuFe catalyst for CO_2 reduction reaction. The underlying cause is that the binary CuFe catalyst can initially activate the stable CO_2 molecule and reduce the high energy barrier, which is in excellent agreement with the theoretical calculation. At potentials more positive than −0.4 V, the driving force is sufficient for hydrogen production but not for overcoming the high energy barrier for methane synthesis. Methane was hence not formed. As the potential shifts negatively, Faradaic efficiency of CH_4 formation is continuously improved with the increasing driving force and approaches a maximum of 51% at −1.2 V. A more negative potential, however, leads to a mild reduction in Faradaic efficiency to 42% because of the severe competition of hydrogen evolution under high overpotential as well as the CO_2 mass transport limitation (55, 56).

High turnover frequency is one distinct highlight of this work. As shown in Fig. 3*F*, an appreciable TOF of 9.5 h^{-1} is achieved under standard one-sun illumination at the onset potential of −0.4 V. The negative shift of potential results in increasing TOF. At −1.2 V, a maximum TOF, which is as high as 2,176 h^{-1}, is achieved at a high current density of −38.3 mA·cm^{-2} and high Faradaic efficiency of up to 51% despite a slight reduction at more negative potential. Herein, the superior TOF mainly originates from the unique synergy of Cu and Fe in the binary catalytic system. Additionally, the pronounced sunlight absorption ability and efficient charge carrier extraction of the GaN/Si platform also play an important role, which will be discussed next.

CO_2 Conversion at the Interface over Cu(111) and Fe_xO_y/Cu(111). To gain fundamental insights into what underlines the superior performance of the binary CuFe catalyst, we have studied the reaction pathways, reaction intermediates, potential-determining steps (PDSs), and free-energy diagrams of the catalytic CO_2RR to CH_4 on $Fe_3O_6H_6$/Cu(111) in comparison with those on Cu(111). Fig. 4*A* shows the optimized structures of adsorption configuration for each reaction intermediate on Cu(111) and $Fe_3O_6H_6$/Cu(111). On the $Fe_3O_6H_6$/Cu(111), it was discovered that the interfacial sites directly participate in binding and stabilizing all of the reaction intermediates. Specifically, the O-bound species (*O and *OH) prefer to bind to reduced Fe^{2+} cation in the metal oxide with the $\eta^1 - O_{Fe^{2+}}$ configuration, while, for C- and O-bound species (species bound through both C and O, i.e., *COOH, *CO, *CHO, *CH_2O, and *CH_3O), the metal/oxide interfacial sites are favored with the $\eta^2 - C_{Cu}O_{Fe^{2+}}$ configuration. Consequently, the $Fe_3O_6H_6$/Cu(111) interfacial sites are beneficial for methane synthesis via stabilizing all of the reaction intermediates during the complex 8-electron/proton coupling transfer process (30, 36).

Fig. 4*A* demonstrates the free-energy diagram of the lowest-energy pathways of CO_2 reduction on the Cu(111) and $Fe_3O_6H_6$/Cu(111) under zero electrode potential ($U = 0$ V). For the case of Cu(111), the protonation of CO species (i.e., *CO → *CHO) is the PDS, exhibiting a free-energy change of 0.85 eV. On the other hand, for CO_2 at the interface of $Fe_3O_6H_6$/Cu(111), the PDS remains the same, but with an appreciably reduced free-energy change of 0.51 eV. By increasing the stability of the *CHO species relative to *CO, it is expected that the energy efficiency of PEC reduction of CO_2 on the $Fe_3O_6H_6$/Cu(111) interface would surpass the pure metals, due to the various structures with complementary chemical properties in the metal/oxide interfacial sites that work in synergy to facilitate the CO_2 reduction into CH_4 (39, 42). Meanwhile, it is worth noting that $Fe_3O_6H_6$/Cu(111) may hinder further reaction steps toward oxygen reduction due to an increased free-energy change associated with the proton/electron transfer step of *OH [i.e., *OH protonation to H_2O(g)] in Fig. 4*A*. For this step, the Cu(111) surface requires 0.14 eV, while the $Fe_3O_6H_6$/Cu(111) demands 0.33 eV. Nonetheless, it would not alter the PDSs of the CO_2 reduction on the Cu(111) surface and $Fe_3O_6H_6$/Cu(111) interface with both of them laying in the *CO/*CHO step. Fig. 4*B* shows the corresponding free-energy diagrams of CO_2 reduction at applied electrode potentials of $U = -0.85$ and -0.51 V for the Cu(111) and $Fe_3O_6H_6$/Cu(111), respectively. These 2 electrode potentials are the required voltages for eliminating the free-energy change of the PDSs (*CO/*CHO). It illustrates that the CH_4-forming reaction from CO_2 might occur at -0.85 and -0.51 V (vs. RHE) on the Cu(111) surface and $Fe_3O_6H_6$/Cu(111) interface, respectively. It suggests that, for methane synthesis, the onset potential of $Fe_3O_6H_6$/Cu(111) is

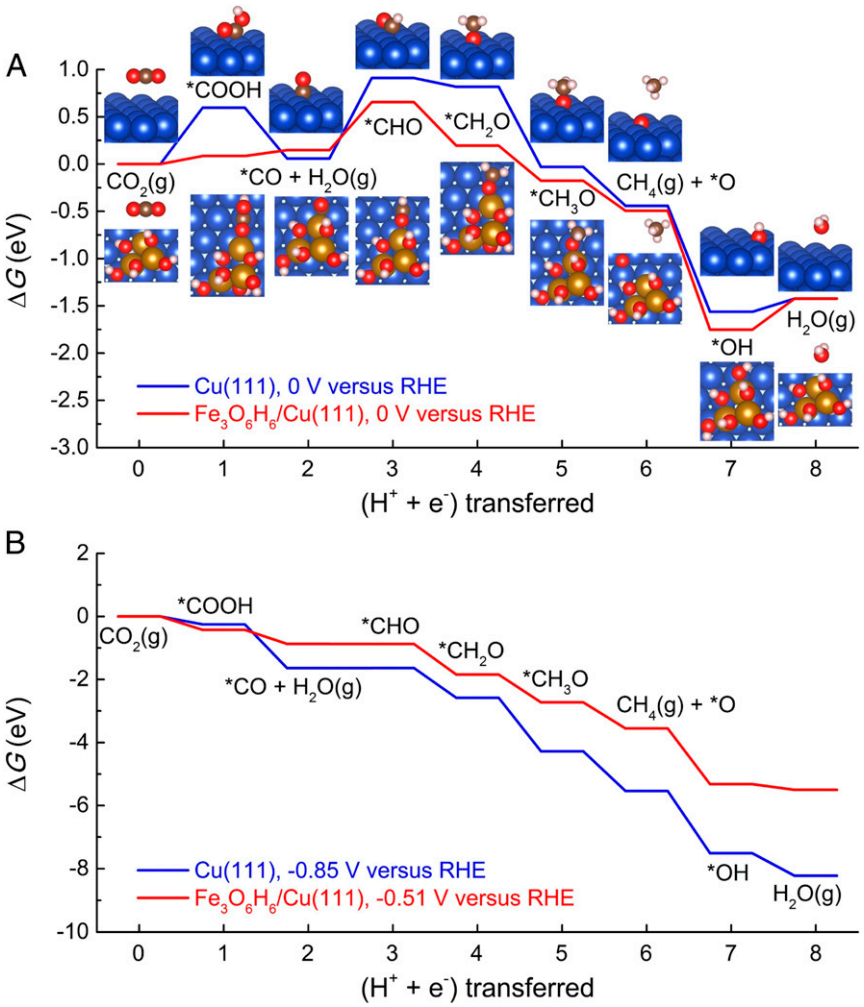

Fig. 4. Calculated free-energy diagrams for CO_2RR on Cu(111) and $Fe_3O_6H_6$/Cu(111) under zero (*A*) and applied electrode potentials (*B*). The values in *B* (i.e., 0.85 and 0.51 eV) show the potential-determining energy barriers that should be overcome for the CH_4 production on Cu(111) and $Fe_3O_6H_6$/Cu(111). Cu, blue; Fe, orange; O, red; C, brown; and H, white.

0.34 V more positive than that of Cu(111), which is in excellent agreement with the experimental results that the onset of the binary CuFe catalyst is 0.3 V lower than that of Cu.

In addition to $Fe_3O_6H_6$/Cu(111), we have also investigated CO_2RR at other possible hydrogenated Fe_xO_y/Cu interfaces, that is, $Fe_3O_3H_3$/Cu(111) and $Fe_6O_7H_7$/Cu(111). The results show that the reaction energetics on $Fe_3O_3H_3$/Cu(111) and $Fe_6O_7H_7$/Cu(111) are similar to that of $Fe_3O_6H_6$/Cu(111) (*SI Appendix*, Fig. S16).

Additionally, to consider the effect of partially oxidization on Cu as characterized in the XPS data, we have also conducted a series of DFT calculations by constructing iron oxide clusters with varying atomic ratios of Fe, Cu, and O on the surface of partially oxidized Cu, that is, Fe_xO_y/Cu_2O(111), similar to the cases of Cu(111). A similar conclusion has been found on the Fe_xO_y/Cu_2O(111) interfaces; that is, in spite of quantitative variations among different systems, the similar qualitative trend confirms the critical role of Fe_xO_y/Cu or Fe_xO_y/Cu_2O(111) interface in activating CO_2 and stabilizing the reaction intermediates to facilitate the CO_2RR for methane synthesis (*SI Appendix*, Fig. S17). Specifically, the CO_2RR on pristine Cu_2O(111) is bottlenecked by the hydrogenation of both *CO to *CHO and *OH to H_2O with a free-energy change for PDS being 1.02 and 1.12 eV, respectively. In contrast, free-energy change of the hydrogenation of *CO to *CHO has been lowered to 0.89, 0.76, and 0.63 eV on $Fe_3O_3H_3$/Cu_2O(111), $Fe_3O_6H_6$/Cu_2O(111), and $Fe_6O_7H_7$/Cu_2O(111), respectively (*SI Appendix*, Fig. S18). And the free-energy change for another PDS of hydrogenation of *OH to H_2O has also been decreased due to a selective destabilization for the reaction intermediate of *OH. It is worth noting that the reaction mechanism of $Fe_xO_yH_z$/Cu_2O(111) is presumably the same as that of $Fe_xO_yH_z$/Cu(111), since all of the reaction intermediates share similar adsorption configurations and react with the Cu atoms on Cu_2O(111) surface.

The Function of GaN NWs. Apart from the catalyst, we also studied the influence of GaN NWs on the excellent performance. In the absence of GaN NWs, CuFe/Si exhibited a planar morphology similar to that of bare silicon substrate (*SI Appendix*, Fig. S19). Control experiments indicate that the *J*–*V* curve of CuFe/Si without GaN NWs is obviously inferior to CuFe@GaN NWs/Si under the same conditions (Fig. 5 *A* and *B*). In particular, the current density of CuFe/Si is only −1.3 mA·cm^{-2} at ∼−1.2 V, which is lower by a factor of 29.5 than −38.3 mA·cm^{-2} for CuFe@GaN NWs/Si (Fig. 5*A*). Meanwhile, the Faradaic efficiency of 16.6% for CuFe/Si is also much lower than that of 51% measured for CuFe@GaN NWs/Si. In consequence, the productivity of CuFe/Si (0.9 μmol·cm^{-2}·h^{-1}) is 2 orders of magnitude less than that of CuFe@GaN NWs/Si (88.9 μmol·cm^{-2}·h^{-1}) (Fig. 5*B*). Both optical and electronic properties were examined to further explore the significant improvement caused by GaN NWs. Ultraviolet-visible (UV-Vis) relative differential reflectance spectra analysis in *SI Appendix*, Fig. S20 shows that GaN NWs enhance the sunlight absorption of the n^+-p silicon junction in a wide wavelength range, due to the light trapping effect (57). In addition, as shown in the energy diagram in *SI Appendix*, Fig. S21, the conduction band edge of GaN and Si is approximately aligned (58), and GaN is nearly defect-free and has high electron mobility. Under illumination, the photogenerated electrons are thus readily extracted from the n^+-p silicon junction and further transferred to the deposited CuFe catalyst in the presence of GaN NWs, which is in good agreement with the electrochemical impedance spectroscopy measurements (*SI Appendix*, Fig. S22). Therefore, it is reasonably concluded that GaN NWs could be an ideal candidate for accelerating the reaction by enhancing the optical and electronic properties, which is consistent with our work using GaN NW for improving the photoelectrocatalytic water splitting performance of MoS_x/Si (59). It is also worth mentioning that, owing to the 1D structure of GaN NW arrays, the catalysis could be spatially decoupled from sunlight collection and charge carriers'

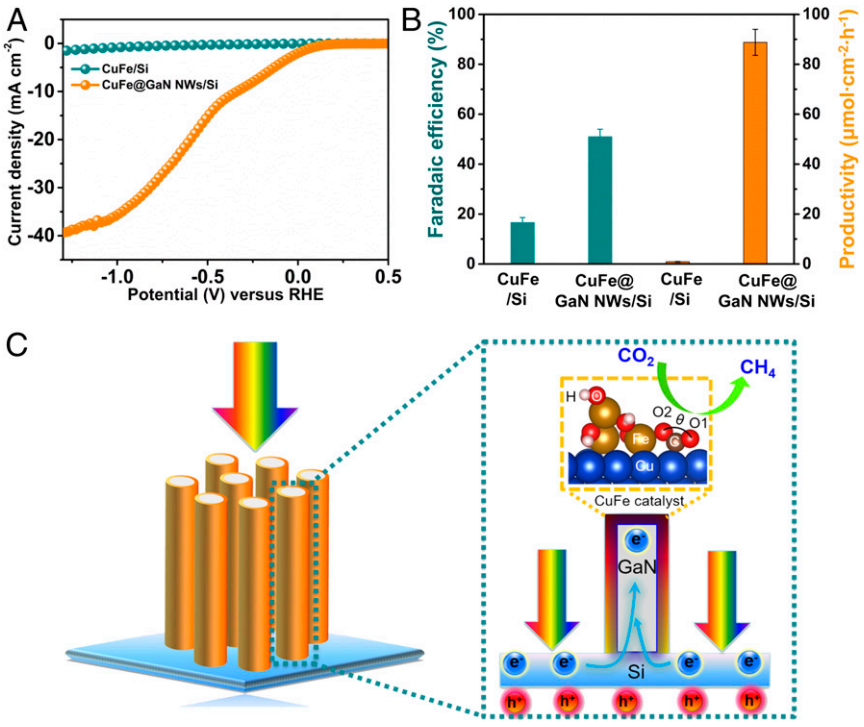

Fig. 5. Role of GaN NWs. *J*–*V* curves (*A*) and Faradaic efficiency and productivity (*B*) of CuFe/Si and CuFe@GaN NWs/Si. Spatial decoupling of CO_2RR from light absorption and charge carriers separation over CuFe@GaN NWs/Si (*C*). Experimental conditions: CO_2-purged 0.5 M $KHCO_3$ aqueous solution (pH ≈ 8), one-sun illumination (AM 1.5G, 100 mW·cm^{-2}).

separation (Fig. 5*C*), which could maximize the synergy of Cu and Fe for methane synthesis by providing sufficient active sites with high atom efficiency.

Isotopic experiments were further conducted to clarify that the methane was produced from CO_2RR. When the reaction was performed in ^{13}C-labeled bicarbonate aqueous solution under the atmosphere of $^{13}CO_2$, gas chromatography (GC) mass spectroscopy analysis only showed a peak at $m/z = 17$ resulting from $^{13}CH_4$ (*SI Appendix*, Fig. S23). The formation of $^{12}CH_4$ was negligible. In contrast, when the blank experiment was carried out in argon-purged Na_2SO_4 aqueous solution, there was no methane synthesized. These results suggest that methane is produced from CO_2. We have further shown that the device can exhibit stable operation of 10 h (*SI Appendix*, Fig. S24). The elemental dissolution of CuFe@GaN NWs/Si into the aqueous solution was not evidently found by ICP, and the morphology of the catalytic architecture remains unchanged (*SI Appendix*, Fig. S25), further confirming the stability of the device.

Conclusions

This work demonstrates that an inexpensive binary CuFe catalyst coupled with GaN NWs on n^+-p silicon wafer is highly active and selective for photoelectrochemical CO_2 reduction toward CH_4. Both experimental and theoretical results suggest that Cu and Fe work in synergy for spontaneous CO_2 activation and conversion with severely deformed CO_2 molecular structure and reduced reaction energy barrier by stabilizing key reaction intermediates. As a result, a high current density of -38.3 mA·cm^{-2} of silicon-based photocathode with a high Faradaic efficiency of 51% and a distinct turnover frequency of 2,176 h^{-1} is achieved for methane synthesis under simulated solar light. The device is manufactured using Earth-abundant materials and is highly stable. This work presents one promising route for producing clean solar fuels from photoelectrocatalytic CO_2 reduction in an aqueous cell.

Materials and Methods

Materials. All of the chemicals were purchased from the commercial companies and utilized without further purification. Distilled water was used thorough the entire process.

Fabrication of Binary CuFe Catalyst over GaN NWs/Si by Electrocatalysis. GaN NWs/Si was first produced as the platform for depositing binary CuFe catalyst. Typically, the polished p-Si (100) wafer was doped using phosphorus and boron as n-type and p-type dopants, respectively, by spin coating. The doped silicon was then annealed at 900 °C under argon atmosphere for 4 h to produce n^+-p silicon junction. The as-prepared n^+-p silicon junction was further employed for plasma-assisted molecular beam epitaxial growth of GaN NWs with germanium as an n-type dopant. The growth was carried out at 790 °C under nitrogen-rich conditions with a nitrogen flow rate of 1.0 cm^3·min^{-1} for 1.5 h. The Ga beam pressure is about 6×10^{-8} torr with a plasma power of 350 W.

In a typical electrodeposition procedure, GaN NWs/Si was immersed into a 3-electrode cell, in which Pt wire and Ag/AgCl were used as counter electrode and reference electrode, respectively. The 200-mL mixture of $CuCl_2$ (≥99%; Sigma-Aldrich) and $FeCl_2$ (99.5%; Alfa-Aesar) aqueous solution with desired concentrations was added into the chamber. Taking the fabrication of $Cu_1Fe_{6.3}$@GaN NWs/Si as an example, 0.1 mmol/L $CuCl_2$ and 0.01 mmol/L $FeCl_2$ were used as the precursors of the CuFe catalyst. The electrodeposition was conducted using cyclic voltammetry at the potential range from +2.5 to −2.5 V versus Ag/AgCl. There are 10 depositing cycles, with a scanning rate of 100 mV/s. The Fe/Cu ratio in the CuFe catalyst can be tailored by tuning the concentration ratio of $FeCl_2$ to $CuCl_2$ in the precursors' solutions while keeping the $CuCl_2$ concentration of 0.1 mmol/L unchanged. The fabricated photoelectrodes were thoroughly rinsed with distilled water and dried with air after the electrodeposition. Both Cu/GaN NWs/Si and Fe/GaN NWs/Si were produced using the same procedure, and the main difference was the precursors used. Moreover, the CuFe catalyst was electrochemically deposited on bare n^+-p silicon junction for a comparison, through the same procedure.

Structure and Optical Characterization. The STEM-HAADF examination was performed by the FEI Titan 80-300-Cube microscope, which is equipped with a high-resolution energy-loss spectrometer of Gatan GIF model 966 (Canadian Center for Electron Microscopy in McMaster University). The SEM images were recorded on an Inspect F-50 Facility for Electron-SEM system. The content of the CuFe catalysts with various Fe/Cu ratios was determined by a Thermo Scientific iCAP 6000 Series ICP-AES. A Thermo Scientific K-Alpha XPS system with a monochromatic Al Kα source was employed for measuring the elemental oxidation states. The optical properties were analyzed by a Cary 5000 UV-Vis-NIR spectrophotometer. The CO_2 adsorption capacity was measured on Autosorb iQ Station 1.

Photoelectrochemical Reaction. The photoelectrochemical CO_2 reduction reaction was carried out in 0.5 M $KHCO_3$ (Sigma-Aldrich) aqueous solution under one-sun solar illumination (Oriel LCS-100). The working electrode, Pt counter electrode, and Ag/AgCl reference electrode were spatially separated by proton exchange membrane. Prior to PEC CO_2RR experiments, 50 mL of electrolyte was added into the cell and then was purged with high-purity CO_2 for at least 20 min. The geometric surface area of the working electrodes is about 0.2 to 0.3 cm^2, and both TOF and productivity were calculated on the basis of the geometric surface area of the working electrodes. The data were recorded on an Interface 1000 E potentiostat (Gamry Instruments). The gas-phase products were quantified using a GC equipped with a thermal conductivity detector (GC 2010; Shimadzu) and a flame ionization detector (GC 2014; Shimadzu). The liquid products were analyzed by NMR spectroscopy (NMR 500 M; Bruker) using 1,3,5-trioxane as an internal standard. In the isotopic experiment, high-purity ^{13}C-labeled bicarbonate (98% atom% 13C; Sigma-Aldrich) aqueous solution was used as the electrolyte. And the reaction was conducted under the atmosphere of high-purity $^{13}CO_2$ (≤100%; Sigma-Aldrich). The isotopic ^{13}C-labeled CH_4 was determined using Agilent G1701DA GC, which is equipped with MSD5973 inert mass spectrometer.

The Equations for Calculating the Productivity and TOF of Methane.

$$\text{Productivity} = \frac{\text{Produced amout of methane}}{(\text{Surface of electrode} \times \text{reaction time})}$$

$$\text{TOF} = \frac{\text{Produced amout of methane}}{(\text{Surface} \times \text{loading density of cocatalysts} \times \text{reaction time})}.$$

Theoretical Section.

Computational methods. Spin-polarized DFT (60, 61) calculations were performed using Vienna Ab-initio Simulation Package (62) software to study the CO_2RR on CuFe@GaN NWs/n^+-p Si. The interaction between the ionic core and the valence electrons was described by the projector augmented wave method (63), and the valence electrons with a plane wave basis up to an energy cutoff of 400 eV and the valence electrons were described with a plane wave basis up to an energy cutoff of 400 eV. The Fe_xO_y/Cu(111) and Fe_xO_y/Cu_2O(111) interfaces were modeled by depositing 3 small iron oxide clusters (i.e., Fe_3O_3, Fe_3O_6, and Fe_6O_7) on 6 × 6 Cu(111) and 3 × 3 Cu_2O(111) surfaces with 3 layers, respectively. The fully hydroxylated iron oxide clusters ($Fe_3O_3H_3$, $Fe_3O_6H_6$, and $Fe_6O_7H_7$) were considered in the calculations to account for the effect of negative applied potentials and aqueous media conditions in PEC CO_2RR (37, 38). The Brillouin zone was sampled using a 2 × 2 × 1 *k*-point grid in the Monkhorst–Pack scheme (64). The Gaussian smearing method with a finite temperature width of 0.05 eV was chosen to improve the convergence of states near the Fermi level. A 15-Å-thick vacuum was added along the direction perpendicular to the surface in the initial slab model to avoid the artificial interactions between the slab and its periodic images. During the geometry optimization, the atoms in the top 2 layers of Cu(111) and Cu_2O(111) along with the adsorbates were allowed to relax, while all other atoms were fixed. The geometry optimizations were considered to reach the convergence until the Hellman–Feynman force on each ion was smaller than 0.02 eV·Å^{-1}. The convergence criteria for the electronic structure was set to 10^{-5} eV per atom. The DFT-D3 method with Becke–Johnson damping was also applied for a better description of weak van der Waals interactions.

Absorbate Energies. The free energies of CO_2 hydrogenation intermediates in electrochemical reaction pathways were calculated by the computational hydrogen electrode (CHE) model suggested by Nørskov et al. (65). By employing the CHE model, a proton/electron ($H^+ + e^-$) in solution can be directly treated, and the effect of a bias can be applied by shifting ΔG by $+neU$, where n is the number of proton–electron pairs transferred, e is the elementary positive charge, and U is the applied potential. The free-energy change (ΔG) is calculated as $\Delta G = \Delta E + \Delta ZPE + \int \Delta C_p dT - T\Delta S$ where ΔE is

the total energy directly obtained from DFT calculations, ΔZPE is the change in zero-point energy, ΔCp is the change in heat capacity, T is temperature, and ΔS is the change in entropy. The temperature is set to 298.15 K to compare current DFT results with the experimental data. The contributions to the free energy for each adsorbate involved in the lowest-energy pathways are listed in *SI Appendix*, Table S2. We also include the solvation corrections which have been found in previous studies, that hydroxyl adsorbates (*OH) exposed to the liquid water were found to be stabilized by ~0.5 eV (65, 66), and hydroxyl that is indirectly bound to the surface through other atoms, *R-OH, may be stabilized by 0.25 eV (as shown for *COOH), as well as a CO* stabilization of 0.1 eV which was applied to CO* and CHO* (67).

Nonadsorbed Species and Gas-Phase Correction. DFT calculations of nonadsorbed species were performed using the same techniques as described above for adsorbed species, except with a Fermi-level smearing of 0.01 eV. The components of the energy calculations for all nonadsorbed species are also listed in *SI Appendix*, Table S2.

Fe_xO_y/Cu and Its Hydroxylation. The inverse Fe_xO_y/Cu(111) models were implemented to describe the Cu/Fe_xO_y interfaces, where a series of iron oxide clusters were deposited on the Cu(111) surface (details of the models are presented in *Computational methods*). Such an inverse model has been suggested to be proper to describe the catalytic behaviors of metal/oxide interfaces under CO_2 hydrogenation conditions (68, 69). Despite the fact that these oxide clusters are of very small size, they possess key structural characteristics and, in particular, the low coordinated sites of the interface structures. As such, it has been suggested that they provide valid representative models to interpret and describe the experimentally observed catalytic activities of metal/oxide interfaces toward CO_2 hydrogenation (38, 70). Moreover, although the H_2 dissociation is a facile process on the Cu(111) surface (71), the dissociated *H cannot strongly adsorb on the Cu(111) surface and would thus recombine and desorb as H_2. As a result, it is expected that the spillover of O atoms saturated by H atoms to form OH groups is favored in the presence of oxide clusters on Cu(111). These results are in good agreement with previous studies that consider metal particles interfacing with other transition metal oxides, such as TiO_2, ZrO_2, and ZnO (36, 39, 44, 72).

Using Fe_3O_6/Cu as a representative example, we further examined the spillover effect by saturating all 6 O atoms in the Fe_3O_6 cluster with H atoms (Fig. 4*A*). The H saturation effectively prevents O atoms from interacting with the Cu(111) surface, instead rendering the $Fe_3O_6H_6$ cluster bound to the Cu(111) surface via the Fe−Cu bond, with a large binding energy of −4.93 eV. Such strong interaction is further evidenced by the charge transfer analysis (73, 74) which reveals a 0.36 e transfer from the undercoordinated Fe atom in $Fe_3O_6H_6$ cluster to Cu(111).

Data Availability. All of the necessary data can be found in *SI Appendix*.

ACKNOWLEDGMENTS. We are grateful for the financial support from Emissions Reduction Alberta, and from the University of Michigan College of Engineering Blue Sky Research Program. P.O. and J.S. thank Natural Science and Engineering Research Council of Canada (NSERC) Discovery Grant RGPIN-2017-05187 and NSERC Strategic Grant STPGP 494012-16, McGill Engineering Doctoral Award, and the Supercomputer Consortium Laval Université du Québec à Montréal (UQAM) McGill and Eastern Quebec. G.B. and S.C. thank NSERC, the Canada Foundation for Innovation, and McMaster University.

1. B. Shan *et al*., Binary molecular-semiconductor p-n junctions for photoelectrocatalytic CO_2 reduction. *Nat. Energy* **4**, 290–299 (2019).
2. M. Schreier *et al*., Solar conversion of CO_2 to CO using Earth-abundant electrocatalysts prepared by atomic layer modification of CuO. *Nat. Energy* **2**, 17087 (2017).
3. J. L. White *et al*., Light-driven heterogeneous reduction of carbon dioxide: Photocatalysts and photoelectrodes. *Chem. Rev.* **115**, 12888–12935 (2015).
4. T. Inoue, A. Fujishima, S. Konishi, K. Honda, Photoelectrocatalytic reduction of carbon dioxide in aqueous suspensions of semiconductor powders. *Nature* **277**, 637–638 (1979).
5. J. Ran, M. Jaroniec, S. Z. Qiao, Cocatalysts in semiconductor-based photocatalytic CO_2 reduction: Achievements, challenges, and opportunities. *Adv. Mater.* **30**, 1704649 (2018).
6. X. Li, J. Yu, M. Jaroniec, X. Chen, Cocatalysts for selective photoreduction of CO_2 into solar fuels. *Chem. Rev.* **119**, 3962–4179 (2019).
7. L. Zhang, Z. J. Zhao, J. Gong, Nanostructured materials for heterogeneous electrocatalytic CO_2 reduction and their related reaction mechanism. *Angew. Chem. Int. Ed. Engl.* **56**, 11326–11353 (2017).
8. D. Bongartz *et al*., Comparison of light-duty transportation fuels produced from renewable hydrogen and green carbon dioxide. *Appl. Energy* **231**, 757–767 (2018).
9. K. P. Kuhl *et al*., Electrocatalytic conversion of carbon dioxide to methane and methanol on transition metal surfaces. *J. Am. Chem. Soc.* **136**, 14107–14113 (2014).
10. F. Marques Mota, D. H. Kim, From CO_2 methanation to ambitious long-chain hydrocarbons: Alternative fuels paving the path to sustainability. *Chem. Soc. Rev.* **48**, 205–259 (2019).
11. H. Rao, C. H. Lim, J. Bonin, G. M. Miyake, M. Robert, Visible-light-driven conversion of CO_2 to CH_4 with an organic sensitizer and an iron porphyrin catalyst. *J. Am. Chem. Soc.* **140**, 17830–17834 (2018).
12. D. D. Zhu, J. L. Liu, S. Z. Qiao, Recent advances in inorganic heterogeneous electrocatalysts for reduction of carbon dioxide. *Adv. Mater.* **28**, 3423–3452 (2016).
13. Z. Weng *et al*., Electrochemical CO_2 reduction to hydrocarbons on a heterogeneous molecular Cu catalyst in aqueous solution. *J. Am. Chem. Soc.* **138**, 8076–8079 (2016).
14. S. Lin *et al*., Covalent organic frameworks comprising cobalt porphyrins for catalytic CO_2 reduction in water. *Science* **349**, 1208–1213 (2015).
15. C. Liu *et al*., Nanowire-bacteria hybrids for unassisted solar carbon dioxide fixation to value-added chemicals. *Nano Lett.* **15**, 3634–3639 (2015).
16. K. K. Sakimoto, A. B. Wong, P. Yang, Self-photosensitization of nonphotosynthetic bacteria for solar-to-chemical production. *Science* **351**, 74–77 (2016).
17. B. A. Rosen *et al*., Ionic liquid-mediated selective conversion of CO_2 to CO at low overpotentials. *Science* **334**, 643–644 (2011).
18. S. Liu *et al*., Shape-dependent electrocatalytic reduction of CO_2 to CO on triangular silver nanoplates. *J. Am. Chem. Soc.* **139**, 2160–2163 (2017).
19. M. Asadi *et al*., Nanostructured transition metal dichalcogenide electrocatalysts for CO_2 reduction in ionic liquid. *Science* **353**, 467–470 (2016).
20. B. W. Zhou *et al*., Mo-Bi-Cd ternary metal chalcogenides: Highly efficient photocatalyst for CO_2 reduction to formic acid under visible light. *ACS Sustain. Chem. Eng.* **6**, 5754–5759 (2018).
21. K. J. P. Schouten, Y. Kwon, C. J. M. van der Ham, Z. Qin, M. T. M. Koper, A new mechanism for the selectivity to C1 and C2 species in the electrochemical reduction of carbon dioxide on copper electrodes. *Chem. Sci.* **2**, 1902–1909 (2011).
22. K. P. Kuhl, E. R. Cave, D. N. Abram, T. F. Jaramillo, New insights into the electrochemical reduction of carbon dioxide on metallic copper surfaces. *Energy Environ. Sci.* **5**, 7050–7059 (2012).
23. A. A. Peterson, F. Abild-Pedersen, F. Studt, J. Rossmeisl, J. K. Norskov, How copper catalyzes the electroreduction of carbon dioxide into hydrocarbon fuels. *Energy Environ. Sci.* **3**, 1311–1315 (2010).
24. R. Reske, H. Mistry, F. Behafarid, B. Roldan Cuenya, P. Strasser, Particle size effects in the catalytic electroreduction of CO_2 on Cu nanoparticles. *J. Am. Chem. Soc.* **136**, 6978–6986 (2014).
25. Y. Li *et al*., Structure-sensitive CO_2 electroreduction to hydrocarbons on ultrathin 5-fold twinned copper wires. *Nano Lett.* **17**, 1312–1317 (2017).
26. S. Y. Zhang, H. L. Zhu, Y. Q. Zheng, Surface modification of CuO nanoflake with Co_3O_4 nanowire for oxygen evolution reaction and electrocatalytic reduction of CO_2 in water to syngas. *Electrochim. Acta* **299**, 282–288 (2019).
27. C. W. Li, J. Ciston, M. W. Kanan, Electroreduction of carbon monoxide to liquid fuel on oxide-derived nanocrystalline copper. *Nature* **508**, 504–507 (2014).
28. Y. Wang *et al*., A monolithically integrated gallium nitride nanowire/silicon solar cell photocathode for selective carbon dioxide reduction to methane. *Chem. Eur. J.* **22**, 8809–8813 (2016).
29. R. Hinogami, Y. Nakamura, S. Yae, Y. Nakato, An approach to ideal semiconductor electrodes for efficient photoelectrochemical reduction of carbon dioxide by modification with small metal particles. *J. Phys. Chem. B* **102**, 974–980 (1998).
30. M. Behrens *et al*., The active site of methanol synthesis over Cu/ZnO/Al_2O_3 industrial catalysts. *Science* **336**, 893–897 (2012).
31. Y. X. Yang, M. G. White, P. Liu, Theoretical study of methanol synthesis from CO_2 hydrogenation on metal-doped Cu(111) surfaces. *J. Phys. Chem. C* **116**, 248–256 (2012).
32. X. Nie, M. R. Esopi, M. J. Janik, A. Asthagiri, Selectivity of CO_2 reduction on copper electrodes: The role of the kinetics of elementary steps. *Angew. Chem. Int. Ed. Engl.* **52**, 2459–2462 (2013).
33. S. Chu *et al*., Tunable syngas production from CO_2 and H_2O in an aqueous photoelectrochemical cell. *Angew. Chem. Int. Ed.* **55**, 14260–14264 (2016).
34. Q. Kong *et al*., Directed assembly of nanoparticle catalysts on nanowire photoelectrodes for photoelectrochemical CO_2 reduction. *Nano Lett.* **16**, 5675–5680 (2016).
35. G. Yin *et al*., Selective electro- or photo-reduction of carbon dioxide to formic acid using a Cu-Zn alloy catalyst. *J. Mater. Chem. A* **5**, 12113–12119 (2017).
36. J. Graciani *et al*., Highly active copper-ceria and copper-ceria-titania catalysts for methanol synthesis from CO_2. *Science* **345**, 546–550 (2014).
37. D. Gao *et al*., Enhancing CO_2 electroreduction with the metal-oxide interface. *J. Am. Chem. Soc.* **139**, 5652–5655 (2017).
38. S. Kattel, B. Yan, Y. Yang, J. G. Chen, P. Liu, Optimizing binding energies of key intermediates for CO_2 hydrogenation to methanol over oxide-supported Copper. *J. Am. Chem. Soc.* **138**, 12440–12450 (2016).
39. S. Chu *et al*., Photoelectrochemical CO_2 reduction into syngas with the metal/oxide interface. *J. Am. Chem. Soc.* **140**, 7869–7877 (2018).
40. L. R. Baker *et al*., Furfuraldehyde hydrogenation on titanium oxide-supported platinum nanoparticles studied by sum frequency generation vibrational spectroscopy: Acid-base catalysis explains the molecular origin of strong metal-support interactions. *J. Am. Chem. Soc.* **134**, 14208–14216 (2012).
41. S. Huygh, A. Bogaerts, E. C. Neyts, How oxygen vacancies activate CO_2 dissociation on TiO_2 anatase (001). *J. Phys. Chem. C* **120**, 21659–21669 (2016).
42. S. Kattel, P. J. Ramírez, J. G. Chen, J. A. Rodriguez, P. Liu, Active sites for CO_2 hydrogenation to methanol on Cu/ZnO catalysts. *Science* **355**, 1296–1299 (2017).
43. S. Kattel, P. Liu, J. G. Chen, Tuning selectivity of CO_2 hydrogenation reactions at the metal/oxide interface. *J. Am. Chem. Soc.* **139**, 9739–9754 (2017).

44. J. A. Rodriguez *et al*., Hydrogenation of CO_2 to methanol: Importance of metal-oxide and metal-carbide interfaces in the activation of CO_2. *ACS Catal.* **5**, 6696–6706 (2015).
45. C. Liu, N. P. Dasgupta, P. D. Yang, Semiconductor nanowires for artificial photosynthesis. *Chem. Mater.* **26**, 415–422 (2014).
46. J. J. Xie *et al*., Highly selective oxidation of methane to methanol at ambient conditions by titanium dioxide-supported iron species. *Nat Catal* **1**, 889–896 (2018).
47. Y. F. Wang, P. Han, X. M. Lv, L. J. Zhang, G. F. Zheng, Defect and interface engineering for aqueous electrocatalytic CO_2 reduction. *Joule* **2**, 2551–2582 (2018).
48. M. Moshe, I. Levin, H. Aharoni, R. Kupferman, E. Sharon, Geometry and mechanics of two-dimensional defects in amorphous materials. *Proc. Natl. Acad. Sci. U.S.A.* **112**, 10873–10878 (2015).
49. H. X. Zhang *et al*., A p-Si/NiCoSe$_x$ core/shell nanopillar array photocathode for enhanced photoelectrochemical hydrogen production. *Energy Environ. Sci.* **9**, 3113–3119 (2016).
50. L. Li *et al*., Nitrogen photofixation over III-nitride nanowires assisted by ruthenium clusters of low atomicity. *Angew. Chem. Int. Ed. Engl.* **56**, 8701–8705 (2017).
51. J. P. Espinos *et al*., Interface effects for Cu, CuO, and Cu_2O deposited on SiO_2 and ZrO_2. XPS determination of the valence state of copper in Cu/SiO_2 and Cu/ZrO_2 catalysts. *J. Phys. Chem. B* **106**, 6921–6929 (2002).
52. J. Y. Park, L. R. Baker, G. A. Somorjai, Role of hot electrons and metal-oxide interfaces in surface chemistry and catalytic reactions. *Chem. Rev.* **115**, 2781–2817 (2015).
53. Q. Ding *et al*., Efficient photoelectrochemical hydrogen generation using heterostructures of Si and chemically exfoliated metallic MoS_2. *J. Am. Chem. Soc.* **136**, 8504–8507 (2014).
54. M. Bernal *et al*., CO_2 electroreduction on copper-cobalt nanoparticles: Size and composition effect. *Nano Energy* **53**, 27–36 (2018).
55. D. Ren, J. Fong, B. S. Yeo, The effects of currents and potentials on the selectivities of copper toward carbon dioxide electroreduction. *Nat. Commun.* **9**, 925 (2018).
56. M. R. Singh, E. L. Clark, A. T. Bell, Effects of electrolyte, catalyst, and membrane composition and operating conditions on the performance of solar-driven electrochemical reduction of carbon dioxide. *Phys. Chem. Chem. Phys.* **17**, 18924–18936 (2015).
57. Y. S. Park, J. S. Lee, Correlating light absorption with various nanostructure geometries in vertically aligned silicon nanowire arrays. *ACS Photonics* **4**, 2587–2594 (2017).
58. S. Vanka *et al*., High efficiency Si photocathode protected by multifunctional GaN nanostructures. *Nano Lett.* **18**, 6530–6537 (2018).
59. B. Zhou *et al*., Gallium nitride nanowire as a linker of molybdenum sulfides and silicon for photoelectrocatalytic water splitting. *Nat. Commun.* **9**, 3856 (2018).
60. P. Hohenberg, W. Kohn, Inhomogeneous electron gas. *Phys. Rev.* **136**, B864 (1964).
61. W. Kohn, L. J. Sham, Self-consistent equations including exchange and correlation effects. *Phys. Rev.* **140**, A1133 (1965).
62. G. Kresse, J. Furthmüller, Efficient iterative schemes for ab initio total-energy calculations using a plane-wave basis set. *Phys. Rev. B Condens. Matter* **54**, 11169–11186 (1996).
63. G. Kresse, D. Joubert, From ultrasoft pseudopotentials to the projector augmented-wave method. *Phys. Rev. B Condens. Matter Mater. Phys.* **59**, 1758 (1999).
64. H. J. Monkhorst, J. D. Pack, Special points for Brillouin-zone integrations. *Phys Rev B* **3**, 5188 (1976).
65. J. K. Nørskov *et al*., Origin of the overpotential for oxygen reduction at a fuel-cell cathode. *J. Phys. Chem. B* **108**, 17886–17892 (2004).
66. G. S. Karlberg, G. Wahnström, Density-functional based modeling of the intermediate in the water production reaction on Pt(111). *Phys. Rev. Lett.* **92**, 136103 (2004).
67. V. Tripković, E. Skúlason, S. Siahrostami, J. K. Nørskov, J. Rossmeisl, The oxygen reduction reaction mechanism on Pt(111) from density functional theory calculations. *Electrochim. Acta* **55**, 7975–7981 (2010).
68. T. Lunkenbein, J. Schumann, M. Behrens, R. Schlögl, M. G. Willinger, Formation of a ZnO overlayer in industrial Cu/ZnO/Al_2 O_3 catalysts induced by strong metal-support interactions. *Angew. Chem. Int. Ed. Engl.* **54**, 4544–4548 (2015).
69. L. N. Zhai *et al*., Titania-modified silver electrocatalyt for selective CO_2 reduction to CH_3OH and CH_4 from DFT study. *J. Phys. Chem. C* **121**, 16275–16282 (2017).
70. S. Kattel *et al*., CO_2 hydrogenation over oxide-supported PtCo catalysts: The role of the oxide support in determining the product selectivity. *Angew. Chem. Int. Ed. Engl.* **55**, 7968–7973 (2016).
71. S. Sakong, A. Gross, Dissociative adsorption of hydrogen on strained Cu surfaces. *Surf. Sci.* **525**, 107–118 (2003).
72. S. Kattel, B. Yan, J. G. Chen, P. Liu, CO_2 hydrogenation on Pt, Pt/SiO_2, and Pt/TiO_2: Importance of synergy between Pt and oxide support. *J. Catal.* **343**, 115–126 (2016).
73. G. Henkelman, A. Arnaldsson, H. Jónsson, A fast and robust algorithm for Bader decomposition of charge density. *Comput. Mater. Sci.* **36**, 354–360 (2006).
74. E. Sanville, S. D. Kenny, R. Smith, G. Henkelman, Improved grid-based algorithm for Bader charge allocation. *J. Comput. Chem.* **28**, 899–908 (2007).